

Exploring Structural and Electrochemical Properties of Li_3TiCl_6 : A Machine Learning Molecular Dynamics Study

Selva Chandrasekaran Selvaraj,^{1,2} Volodymyr Koverga,^{1,2} and Anh T. Ngo^{1,2,*}

¹*Department of Chemical Engineering, University of Illinois Chicago, Chicago, IL 60608, United States*

²*Materials Science Division, Argonne National Laboratory, Lemont, IL 60439, United States*

(Dated: March 5, 2024)

We performed large-scale molecular dynamics simulations based on a machine-learning force field (MLFF) to investigate the Li-ion transport mechanism in cation-disordered Li_3TiCl_6 cathode at six different temperatures, ranging from 25°C to 100°C. In this work, deep neural network method and data generated by *ab-initio* molecular dynamics (AIMD) simulations were deployed to build a high-fidelity MLFF. Radial distribution functions, Li-ion mean square displacements (MSD), diffusion coefficients, ionic conductivity, activation energy, and crystallographic direction-dependent migration barriers were calculated and compared with corresponding AIMD and experimental data to benchmark the accuracy of the MLFF. From MSD analysis, we captured both the self and distinct parts of Li-ion dynamics. The latter reveals that the Li-ions are involved in anti-correlation motion that was rarely reported for solid-state materials. Similarly, the self and distinct parts of Li-ion dynamics were used to determine Haven's ratio to describe the Li-ion transport mechanism in Li_3TiCl_6 . Obtained trajectory from molecular dynamics infers that the Li-ion transportation is mainly through interstitial hopping which was confirmed by intra- and inter-layer Li-ion displacement with respect to simulation time. Ionic conductivity (1.06 mS/cm) and activation energy (0.29eV) calculated by our simulation are highly comparable with that of experimental values. Overall, the combination of machine-learning methods and AIMD simulations explains the intricate electrochemical properties of the Li_3TiCl_6 cathode with remarkably reduced computational time. Thus, our work strongly suggests that the deep neural network-based MLFF could be a promising method for large-scale complex materials.

I. INTRODUCTION

Addressing the increasing energy demands in the face of climate change concerns requires a sustainable zero-carbon energy future. Rechargeable batteries that are capable of converting electrical energy to chemical energy and vice versa, are pivotal for energy storage in this context. While lithium-ion batteries have proven successful for portable devices, all-solid-state batteries (ASSLBs) present a promising solution for the next generation. ASSLBs offer enhanced safety and a longer lifespan compared to traditional lithium-ion electric vehicle batteries and are aligning with goals for achieving zero-carbon emissions.

In ASSBs, the cathode is a crucial component and it is playing a vital role in determining their overall performance. Particularly, energy storage capacity, voltage, cycle life, safety, cost, and environmental impact, are intricately linked to the cathode material. Among the widely used sulfide- and oxide-based cathode materials, latter take a leading position in energy storage manufacturing. Indeed, such commercial attention is also facilitated by the use of transition metals, including single- LiMO_2 , multi- $\text{LiNi}_{1-x-y}\text{Mn}_x\text{Co}_y\text{O}_2$, and polyanionic-TM-based LiMPO_4 ($M=3d$ -block elements of 3 group; $x=y=0.1$ to 0.33),[1–10] which essentially improve the performance of ASSLB devices. Since the projected annual production of Li-ion batteries is expected to reach several terawatt hours, demand for Fe, Co, and Ni based cathode materials increases rapidly[11]. However, Co and Ni prove to

be expensive. Consequently, ongoing efforts include both simulations and experimental studies, aiming to identify more cost-efficient alternatives for cathodes[12].

Among various studies on cathode materials, a recent research has shown that Li_3TiCl_6 is both cost-effective and outperforms previous benchmarks for ASSLBs[13]. However, the experimental investigation [13] of Li_3TiCl_6 falls short of providing a comprehensive understanding of the underlying physics and chemistry governing the Li-ion transport mechanism, which is a key factor to determine the performance entire battery. Thus, we turn to atomic simulation techniques to study the underlying Li-ion transport mechanism in Li_3TiCl_6 .

The conventional atomic simulation based on density functional theory (DFT) is well known for predicting structural, electrochemical, and Li-ion transport properties [12, 14] with few hundred atoms. Nevertheless, it requires extensive computational resources and is helpless for large-scale demand posed by Li-ion intercalation-driven electrochemical studies. To facilitate this challenge, various machine learning (ML) methods are utilized in conjunction with molecular dynamics simulations[15, 16]. Among the variety of ML techniques, e.g., artificial neural networks,[17, 18] kernel-based methods,[19], Gaussian approximation potentials,[20] and atomic cluster expansion,[21] Deep Learning Potential (DLP) stands out as versatile tool, capable of producing accurate potential models on the basis of quantum-chemical calculations [22, 23].

Therefore, our approach in this work involves the inte-

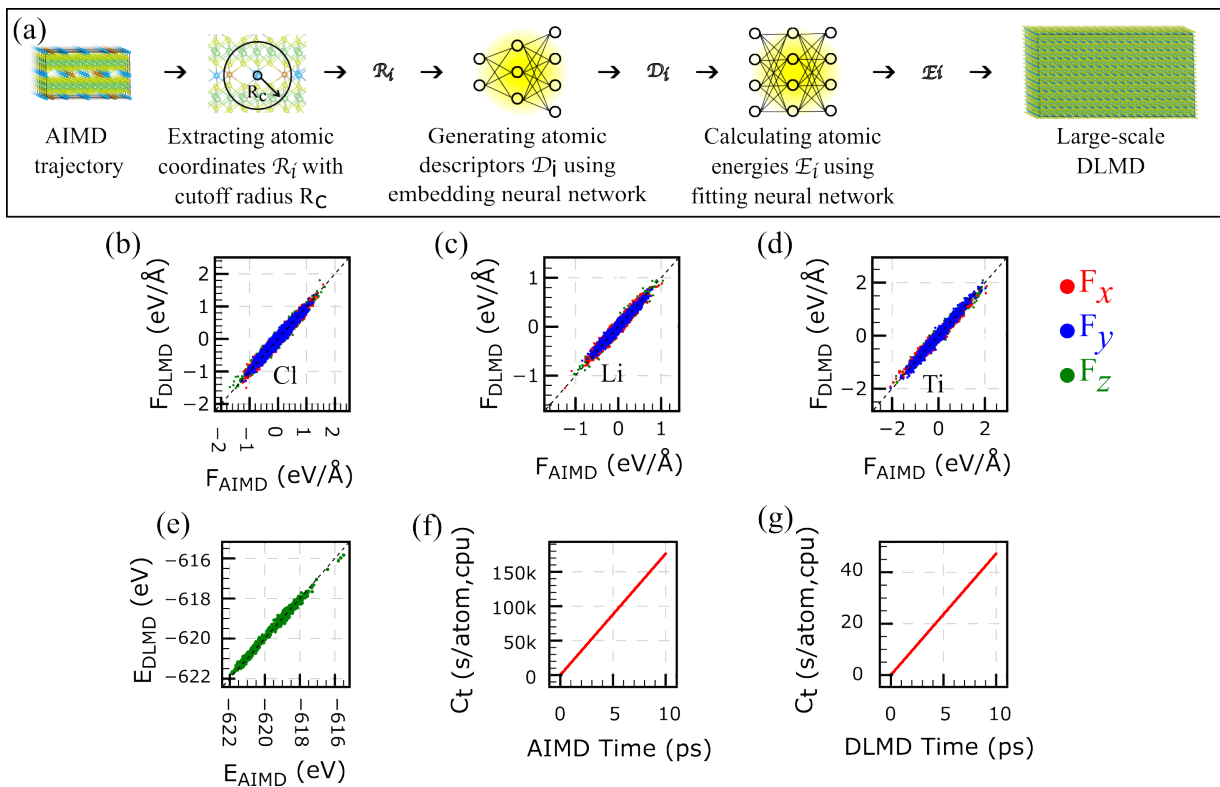


FIG. 1. (a) Schematic diagram of the protocol of DLMD development (see Section 2 for the details). (b-d) DLMD predicted forces corresponding to AIMD forces for Cl (b), Li (c) and Ti (d) elements, as well as the respective forces along x , y , and z directions. (e) DLMD predicted energies corresponding to AIMD energies. (e-f) Simulation time (C_t) of AIMD(e) and DLMD(f) approaches, respectively.

gration of AIMD, machine learning methods based on deep neural networks, and classical molecular dynamics. This integrated approach is collectively referred to as deep learning molecular dynamics (DLMD) simulations [22, 23] to investigate the structural and Li-ion transport properties of the Li_3TiCl_6 cathode. With this, we organize the manuscript as follows: Section II describes detailed simulation techniques, as illustrated in FIG.1. Section III is composed of results and discussions covering structural parameters, RDF, MSD, self and correlated motion of Li-ion displacement, diffusion coefficient, Li-ion transport mechanism, ionic conductivity, and activation energy of Li_3TiCl_6 . The calculated values of ionic conductivity and activation energy are in good agreement with those of experimental values [13]. Finally, we conclude our results and discussions in Section IV.

II. SIMULATION METHODOLOGIES

A. AIMD simulation

DFT-based calculations were employed to optimize the crystal structure of Li_3TiCl_6 using the Vienna *Ab-initio* Simulation Package (VASP)[24, 25]. The initial structure

of Li_3TiCl_6 in monoclinic cell with $C2/m$ space group for VASP was adopted from experimental results[13]. The projector augmented wave (PAW) formalism described the valence electrons of Li, Cl, and Ti atoms using plane wave-based wave functions was employed[26]. The structure optimization, involving the minimization of ground state energy, utilized the generalized gradient approximation of Perdew and Wang method with different U -parameters[27, 28]. A set of $U - J$ values, 0 and 4eV were chosen to taking into account of strong correlation effect of Ti-3d electrons[29, 30]. A kinetic cutoff energy of 450 eV was set to enhance calculation accuracy. The Brillouin zone of the supercell with 160 and 320 atoms was sampled with $4 \times 2 \times 4$ and $4 \times 2 \times 2$ k -meshes for ionic optimization, respectively. Ionic and electronic optimizations were alternately performed until the forces on each ion reached less than ± 10 meV/Å.

The designed simulation cells were optimized and subjected to AIMD simulations. The time step for the AIMD simulations was set to 1 fs, and the simulations were continued for a duration considered separately within the canonical NVT ensemble to generate the dataset for the DLP model.

TABLE I. The calculated loss function parameter expressed by mean absolute error (MAE) and root mean square error (RMSE) of deep learning potential model

Metric	Value	Unit
Energy MAE	6.723×10^{-4}	eV
Energy RMSE	8.389×10^{-4}	eV
Force MAE	5.959×10^{-3}	eV/Å
Force RMSE	7.827×10^{-3}	eV/Å

B. Deep Learning Potential

The DLP was developed using the deep neural network method implemented in DeePMD-kit (v2.2.7) [31]. The deep neural network algorithm in DeePMD is designed using the TensorFlow Python library [32]. The deep potential-smooth edition (DeepPot-SE), an end-to-end machine learning-based potential energy surface (PES) model, was employed with a cutoff radius of 7 Å to include more neighbour atoms in the featurization process. Indeed, it efficiently represents the PES of a wide variety of systems with the accuracy of *ab-initio* models [33].

In the process of constructing DLP, local coordinate matrix, \mathcal{R} and local atomic environment matrix, $\{\mathcal{R}_{ij}\}_{i=1}^N$ are represented as shown in Eq. (1) and (2).

$$\mathcal{R} = \{\mathbf{r}_1^T, \dots, \mathbf{r}_i^T, \dots, \mathbf{r}_N^T\}^T \quad (1)$$

where $\mathbf{r}_i = (x_i, y_i, z_i)$ which contains 3 Cartesian coordinates of atom and N is total number of atoms. And \mathcal{R} can be transformed into local environment matrices as

$$\{\mathcal{R}_{ij}\}_{i=1}^N = \{\mathbf{r}_{i1}^T, \dots, \mathbf{r}_{i2}^T, \dots, \mathbf{r}_{ij}^T | j \in N_{R_c}(i, R_c = 7.0)\}^T \quad (2)$$

where j and $N_{R_c}(i)$ are indexes and number of neighbors of i^{th} atom within the cut-off radius $r_c = 7.0\text{Å}$, and $\mathbf{r}_{ji} \equiv \mathbf{r}_j - \mathbf{r}_i$ is defined as the relative coordinate.

An embedding neural network with three layers, each containing 32, 64, and 128 neurons, was used to convert the local atomic coordinates ($\mathcal{R} \in \mathbb{R}^{N \times 3}$) into atomic descriptors $\mathcal{D}_i = \mathcal{D}_i(\{\mathcal{R}_{ij}\}_{i=1}^N)$ that preserves the structural symmetries of the system [31, 34]. Descriptor values were input into a fitting neural network with three layers, each comprising 256 neurons, that maps descriptors to atomic energies E_i [31, 34], and thus the total energy and force of each atom in the system are calculated by Eq. (3) and Eq. (4).

$$E = \sum_{i=0}^{i=N} E_i = \sum_{i=0}^{i=N} E(\mathcal{D}_i) \quad (3)$$

$$F_{i,\alpha} = -\frac{\partial E}{\partial r_{i,\alpha}} \quad (4)$$

The hyperbolic tangent (tanh) activation function was applied in the neural network, introducing non-linearity to effectively train the intricate atomic descriptor data \mathcal{D}_i . The training process consisted of 10^4 steps, utilizing mean squared error for both energies and forces as the loss function at each training step. The optimization was facilitated by the Adam optimizer, initiating with a learning rate of 10^{-3} and concluding at 10^{-8} , with a decay parameter set to 5000. With these specified parameters, a dataset comprising 1.3 million training samples and 10000 test samples from diverse trajectories were employed to construct the DLP model. The calculated loss function parameters such as mean absolute error and root mean square error during validation of developed DLP model is tabulated in Table-1. Accuracy of the predicted data of force and energy is more than 99 % and data points of predicted versus trained are shown in FIG.1b to FIG.1e.

C. Deep learning molecular dynamic simulation

Similarly to AIMD conditions, The simulations of DLMD was conducted in the NVT ensemble using the LAMMPS simulation package [35] coupled with the DeepMD plugin [34]. The simulation cell was designed to accommodate 20,000 atoms. Simulations were carried out at six different temperatures—298, 313, 328, 333, 358, and 373 K—controlled by the Nose-Hoover thermostat.

Prior to NVT simulation, the energy minimization was conducted using conjugate gradient algorithm. The temperature damping parameter was set to 100 fs, and a uniform integration time-step of 1 fs was employed for all simulations, extending over a total duration of 5.5 ns. Computing time for AIMD and DLMD simulation for 10 ps per atom on one computing core was calculated and plotted in FIG.1g and FIG.1g, respectively and it reveals that DLMD is 3730 times faster than AIMD simulation. The unit-cell of AIMD simulations were visualized using VESTA software[36] and the trajectories of AIMD and DLMD simulations were visualized using OVITO software.[37]

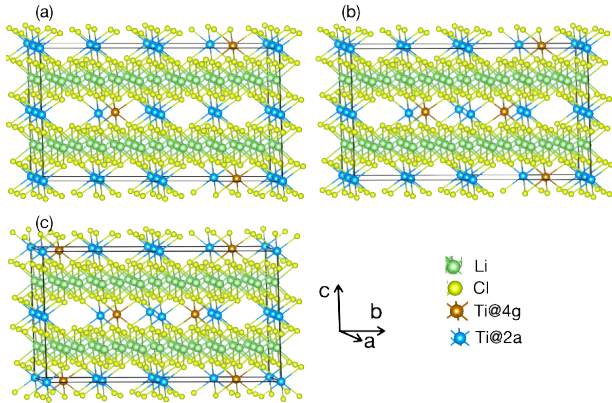
III. RESULTS AND DISCUSSION

A. Radial distribution

The monoclinic simulation cells, comprising 160 and 320 atoms, were employed to create three distinct Ti occupancies at the 2a and 4g sites, aiming to reproduce the experimentally reported structure of Li_3TiCl_6 [13] (FIG.2). The three different occupancies, along with the corresponding experimental Ti occupancy, are summarized in Table-2.

TABLE II. Calculated lattice parameters of monoclinic Li_3TiCl_6 with different Ti occupancy at $4h$ and $2a$ sites.

	0.875Ti@ $2a$ 0.063Ti@ $4g$		0.851Ti@ $2a$ 0.075Ti@ $4g$	0.844Ti@ $2a$ 0.078Ti@ $4g$		0.754Ti@ $2a$ 0.123Ti@ $4g$	0.750Ti@ $2a$ 0.125Ti@ $4g$	
	U_{eff} =0.0	U_{eff} =4.0	Expt [13]	U_{eff} =0.0	U_{eff} =4.0	Expt [13]	U_{eff} =0.0	U_{eff} =4.0
Lattice constant, a (Å)	6.434	6.401	6.350	6.415	6.396	6.350	6.451	6.398
Lattice constant, b (Å)	11.05	10.91	10.88	10.96	11.93	10.89	11.02	10.95
Lattice constant, c (Å)	6.351	6.340	6.337	6.383	6.348	6.353	6.413	6.381
Angle β ($^\circ$)	110.7	110.6	110.2	110.6	110.4	110.1	110.9	110.8

FIG. 2. Ball and stick model of Li_3TiCl_6 structure with three different Ti occupancies at $2a$ and $4g$ sites.

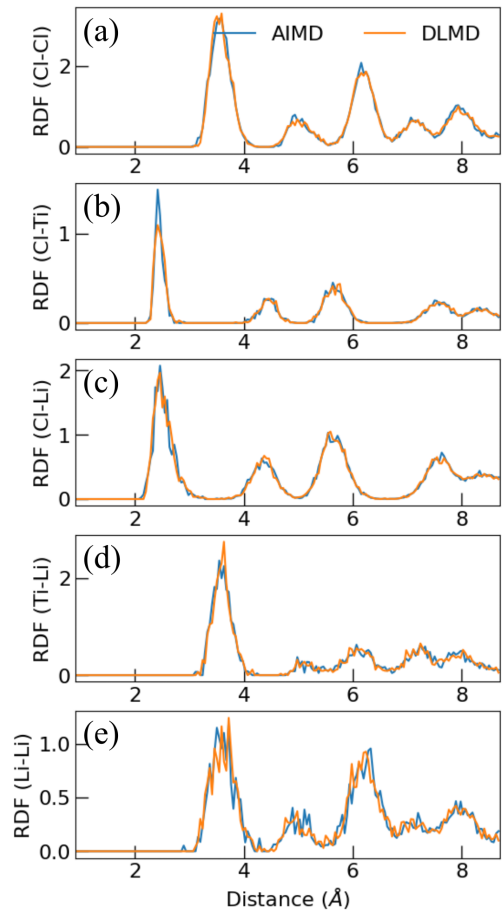
Subsequently, the designed cells underwent optimization, and their structural parameters closely matched experimental values[13] for DFT+U calculation with $U=4.0$ eV. The slight variations, when compared to their experimental values, may be attributed to the small change in the Ti occupancy within the designed simulation cells as well as the overestimation of GGA functional that used in the DFT simulation. Based on the structural optimization results, we selected the Li_3TiCl_6 structure with Ti-sites at 0.754 on $2a$ and 0.123 on $4g$, which represents experimentally annealed structure at 300°C and exhibited a maximum Li-ion conductivity of 1.04 mS/cm at room temperature[13].

Atomic trajectories produced by AIMD and DLMD at 298 K were compared in the framework of radial distribution function (RDF), calculated by the equation given below:

$$g(r) = \frac{1}{N} \sum_{i=1}^N \sum_{j \neq i} \frac{1}{4\pi r_{ij}^2 \Delta r} \delta(r - r_{ij}) \quad (5)$$

where, N , r_{ij} , and Δr represent the total number of atoms in the radius r , the distance between atoms i and j , and the width of each bin, respectively.

Generally, RDFs between pairs of atoms in the same material, estimated using AIMD and DLMD, may provide valuable confirmation of reliability, accuracy, and

FIG. 3. Comparison of radial distribution function of Li_3TiCl_6 analyzed based on AIMD with $U=4.0$ eV and DLMD trajectories at 298K.

consistency in capturing the structural features of the system under investigation. Thus, results of the RDF analyzed using two theoretical approximations for Cl-Ti, Cl-Li, Ti-Li, Li-Li, and Cl-Cl pairs of atoms are presented in FIG.3. As can be clearly seen, all the peak positions, shapes, and heights of RDF obtained by means of DLMD exhibit good agreement with AIMD results, even at larger distance, confirming the ability of DLMD to predict other static properties with high-level accuracy.

Considering the RDF results more carefully, one can

observe multiple peaks along the large separation distances which indicates a relatively high degree of atomic structuring in Li_3TiCl_6 . For Cl-Ti and Cl-Li pairs, the first peak position is nearly the same at a distance of 2.53 Å, while other pair combinations are situated at larger distances of 3.5 Å. At the same time, the height of the Li-Cl peak is greater than that of Ti-Cl, which reveals that a relatively higher probability of Li-Cl interactions compared to Ti-Cl. This is evident when comparing the peak heights of Li-Li, Ti-Li, and Cl-Cl pairs.

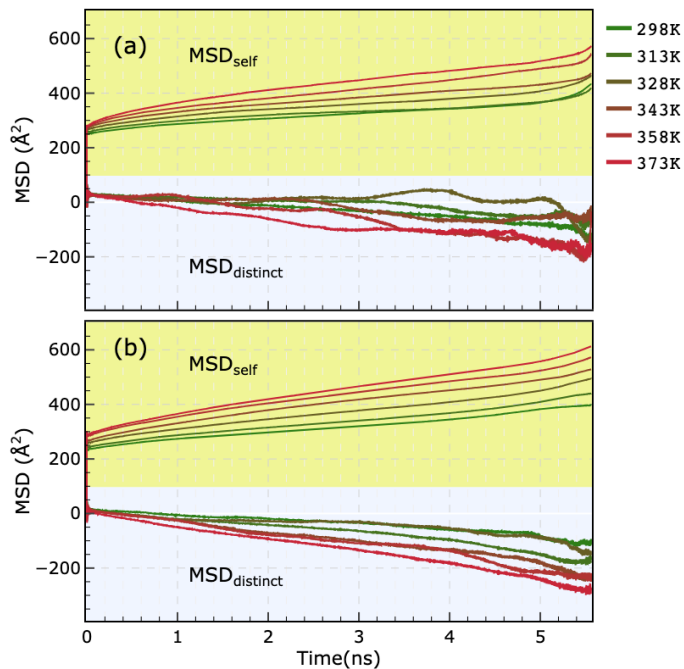


FIG. 4. Time-evolution of mean squared displacement (MSD) of Li atoms calculated at 298, 313, 328, 333, 358, and 373K for uncorrelated, MSD_{self} , and correlated part, $\text{MSD}_{\text{distinct}}$. (a) and (b) are MSDs calculated from DLMD simulation with $U=0.0$ eV and $U = 4.0$ eV, respectively.

B. Diffusion coefficients

The diffusion of Li-ions was determined from DLMD trajectories, where the positions of Li atoms, denoted as $\{\mathbf{r}_i(t)\}_{i=1}^N$, are tracked as a function of time t for all N Li atoms. This involves calculating the mean square displacement of Li atoms, $\text{MSD}_{\text{Total}}$ including correlated motion [38, 39] as follows.

$$\text{MSD}_{\text{Total}} = \lim_{t \rightarrow \infty} \frac{d}{dt} \left\langle \sum_{\alpha, i=1}^N [\mathbf{r}_i^\alpha(t) - \mathbf{r}_i^\alpha(t_0)] \bullet \sum_{\beta, j=1}^N [\mathbf{r}_j^\beta(t) - \mathbf{r}_j^\beta(t_0)] \right\rangle \quad (6)$$

where α and β are Li atoms among N atoms at t and $t_0 = 0$. From above Equation-6, we calculated uncorrelated motion of MSD (MSD_{self}) and correlated motion of MSD ($\text{MSD}_{\text{distinct}}$) as follows

$$\text{MSD}_{\text{self}} = \text{MSD}_{\text{Total}}(\alpha \equiv \beta) \quad (7)$$

$$\text{MSD}_{\text{distinct}} = \text{MSD}_{\text{Total}}(\alpha \neq \beta) \quad (8)$$

When $\text{MSD}_{\text{distinct}} < 0$ describes negative correlation between Li-ions and, hence, negatively affect the Li-ion transport. Based on Equations 6-8, we calculated MSD_{self} and $\text{MSD}_{\text{distinct}}$ and collect the results in FIG.4. It is seen that $\text{MSD}_{\text{distinct}}$ values for Li_3TiCl_6 at different temperatures show negative correlation (or anticorrelation) between Li atoms during their dynamics. To quantify this observation the diffusion coefficient was calculated on the basis of MSD using

$$D = \frac{\text{MSD}(\Delta t)}{2d\Delta t} \quad (9)$$

where d is dimensionless quantity which is equal to 3 for three dimensional transport. Since, Li_3TiCl_6 has anticorrelated Li-ion dynamics, calculated D_{self} is highly overestimated about 14 times of D_{Total} , which is $1.6 \times 10^{-14} \text{cm}^2/\text{s}$ at 298K with DLP generated from DFT+U = 4.00 eV.

One way to understand this phenomenon is by analyzing Haven's ratio (H_R) [40] which is defined as the ratio of the self-diffusion coefficient of Li-ions (D_{self}) to the total diffusion coefficient (D_{Total}) using Eq. 9.

$$H_R = \frac{D_{\text{self}}}{D_{\text{Total}}} \quad (10)$$

Here, D_{self} represents the individual motion of ions which is independent of overall charge transport. On the other hand, D_{Total} is the diffusion coefficient calculated from the material's conductivity by considering the collective motion of ions that contributes to overall charge transport. In the case of uncorrelated Li-ion dynamics, $D_{\text{Total}} \equiv D_{\text{self}}$, and H_R becomes 1. If H_R is less than 1, D_{distinct} should have been positively correlated with Li-ion dynamics, typically observed in liquid and glass electrolytes.[39, 40] In our case, since H_R is greater than one, we propose that Li-ion dynamics may involve an interstitial and/or inter-layer transport mechanism.

C. Transport mechanism

Furthermore, we analyzed the Li-ion path to confirm the inter- and intra-layer diffusion of the ions. Among all the Li atoms in the trajectory simulated at 298 K, we arbitrarily selected two Li atoms to track the ionic motion

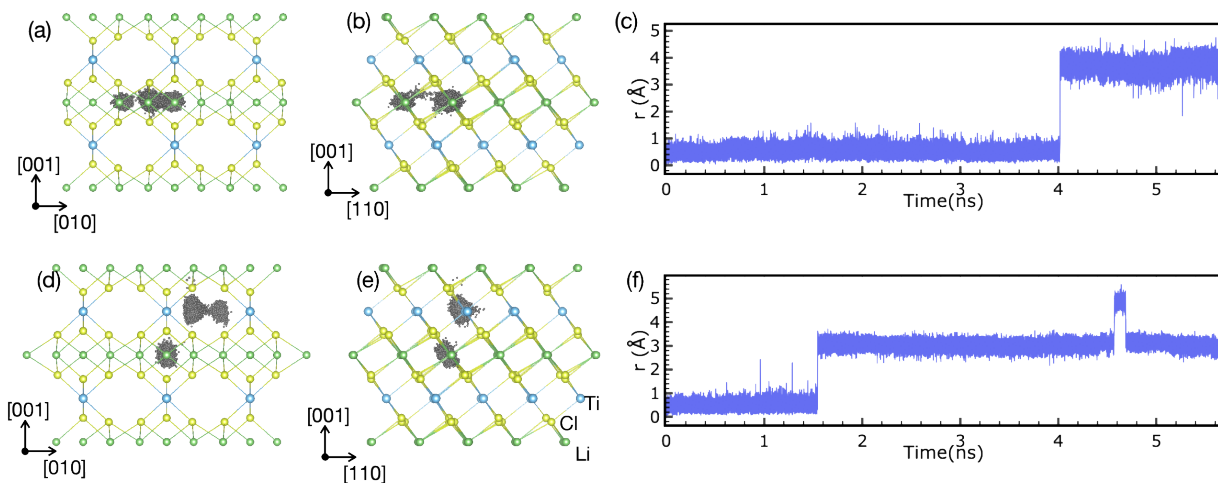


FIG. 5. Illustration of intra-layer Li-ion movement (gray balls) along Li_3TiCl_6 (a) [010], and (b) [110] view-point directions. (c) Time-evolution of Li atom translations corresponding to (a) and (b) as a function of time. Illustration of inter-layer Li-ion movement (gray balls) along Li_3TiCl_6 (d) [010], and (e) [110] view-point directions. (f) Translation distance of Li atoms corresponding to (d) and (e) as a function of time.

over time (in FIG.5). Figures 5a and 5b clearly illustrate the Li atom (gray-colored dots) moving within the Li layer through interstitial hopping. Simultaneously, inter-layer motion between Li- and Ti-layers is also observed through interstitial migration, as shown in Fig. 5d and 5e.

The movements of ionic movement corresponding to intra- and inter-layer migration are shown in Fig. 5c and 5f. More interestingly, Fig. 5f demonstrates that inter-layer Li-ion migration reaches the third cation layer at 4.7 ns through interstitial sites, proving multiple-site hopping of Li-ion. Since the Li_3TiCl_6 crystal structure has partially occupied Ti-2a as well as Ti-4g, the structure possesses inherent voids that can also possibly act as hopping sites for Li-ion migration. Therefore, our study confirms that Li_3TiCl_6 has an inter- and intra-layer interstitial hopping-based Li-ion transport mechanism.

D. Ionic conductivity

The ionic conductivity, denoted as σ , can be determined from the self-diffusion coefficient using the Nernst–Einstein equation[41]:

$$\sigma = \frac{ne^2Z^2}{H_Rk_B T} D_{\text{total}} \quad (11)$$

Here, n represents the ion density of Li, e is the elementary electron charge, Z denotes the valence of Li, and k_B is the Boltzmann constant. The calculated ionic conductivity values from diffusion coefficients align well with experimental values [13], as demonstrated in FIG.6. Additionally, when considering the temperature dependence of ionic conductivity in solid-state electrolytes, high-

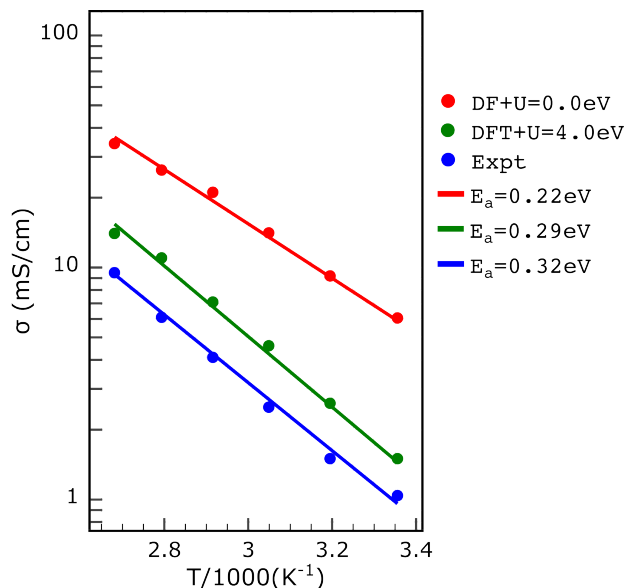


FIG. 6. Arrhenius plot for ionic conductivity as a function of temperature calculated using of DLMD at 298, 313, 328, 333, 358, and 375 K with $U = 0.0$ and $U = 4.0$ eV in comparison with experimental data [13].

temperature ionic conductivities obtained from DLMD simulations can be leveraged to estimate the activation barrier of the electrolytes at lower temperatures using the Arrhenius relationship: $\sigma = \sigma_0 e^{-E_a/(k_B T)}$. The calculated activation energy is 0.29 eV, closely matching the experimental value of 0.32 eV. In addition, Li-ion migration barriers were calculated using the DFT-based NEB method along different crystallographic directions. The barriers along [110], [010], [100] are 0.30, 0.303,

0.312, and 1.14 eV, respectively. The inter-layer ([110] and [101]) migration barriers are considered along interstitial sites and are very close to the activation energy calculated in DLMD simulations. Thus, the calculated activation energy and Li-ion barrier energy confirm the accuracy of both DLMD and DFT simulations, respectively.

IV. CONCLUSION

We performed large-scale and MLFF-driven molecular dynamics simulations to investigate the Li-ion transport mechanism in cation-disordered Li_3TiCl_6 cathode at six different temperatures, ranging from 298K to 373K. Deep neural network method along with data generated by AIMD simulation were used to build a high-fidelity MLFF. Predicting accuracy of atomic forces, energy, and structure by our trained MLFF was confirmed with set of new AIMD data and corresponding RDF. The calculated self and distinct part of Li-ion MSD reveal that the Li-ions are involved in anti-correlation motion that was rarely reported for solid-state materials.

In the same way, analysis of trajectory from DLMD infers that the Li-ion transportation occurs through interstitial hopping which was confirmed by intra- and inter-layer Li-ion movement as a function of simulation time. The temperature dependent ionic conductivity and, thus, activation barrier values for Li_3TiCl_6 demonstrate a decreasing trend with temperature, aligning with typical behavior of ionic conductors. Moreover, activation energy of 0.29 eV, which is in close agreement with experimental result, matches well with inter-layer ionic diffusion barrier calculated by DFT along [110] crystallographic direction. Overall, the combination of machine-learning methods and AIMD simulations elucidates the complex Li-ion electrochemical properties of the Li_3TiCl_6 cathode by significantly reducing computational time. Hence, our work strongly suggests that the MLFF using deep neural networks could be promising for studying large-scale complex materials.

ACKNOWLEDGMENTS

This work was supported by the by the Assistant Secretary for Energy Efficiency and Renewable Energy, Office of Vehicle Technologies of the US Department of Energy, through the Battery Materials Research (BMR) program. We gratefully acknowledge the computing resources provided on Bebop, a high-performance computing cluster operated by the Laboratory Computing Resource Center at Argonne National Laboratory.

CONFLICT OF INTEREST

The authors declare no conflict of interest.

* anhngo@uic.edu

- [1] N. Mohamed and N. K. Allam, Recent advances in the design of cathode materials for li-ion batteries, *RSC Adv.* **10**, 21662 (2020).
- [2] S. B. Chikkannanavar, D. M. Bernardi, and L. Liu, A review of blended cathode materials for use in li-ion batteries, *Journal of Power Sources* **248**, 91 (2014).
- [3] E. Antolini, LiCoO_2 : formation, structure, lithium and oxygen nonstoichiometry, electrochemical behaviour and transport properties, *Solid state ionics* **170**, 159 (2004).
- [4] J. W. Fergus, Recent developments in cathode materials for lithium ion batteries, *Journal of Power Sources* **195**, 939 (2010).
- [5] N. Tran, L. Croguennec, M. Ménétrier, F. Weill, P. Biensan, C. Jordy, and C. Delmas, Mechanisms associated with the “plateau” observed at high voltage for the over-lithiated $\text{Li}_{1.12}(\text{Ni}_{0.425}\text{Mn}_{0.425}\text{Co}_{0.15})_{0.88}\text{O}_2$ system, *Chemistry of Materials* **20**, 4815 (2008).
- [6] S. G. Stewart, V. Srinivasan, and J. Newman, Modeling the performance of lithium-ion batteries and capacitors during hybrid-electric-vehicle operation, *Journal of The Electrochemical Society* **155**, A664 (2008).
- [7] A. Armstrong, A. Robertson, and P. Bruce, Structural transformation on cycling layered li $(\text{Mn}_{1-y}\text{Co}_y)_2\text{O}_2$ cathode materials, *Electrochimica Acta* **45**, 285 (1999).
- [8] D. G. Lee, R. K. Gupta, Y. S. Cho, and K. T. Hwang, Improved electrochemical properties of li $(\text{Ni}_{0.7}\text{Co}_{0.3})_2\text{O}_2$ cathode for lithium ion batteries with controlled sintering conditions, *Journal of applied electrochemistry* **39**, 671 (2009).
- [9] X. Shi, C. Wang, X. Ma, and J. Sun, Synthesis and electrochemical properties of $\text{LiNi}_{0.9}\text{Co}_{0.1}\text{O}_2$ cathode material for lithium secondary battery, *Materials Chemistry and Physics* **113**, 780 (2009).
- [10] A. Yamada, S.-C. Chung, and K. Hinokuma, Optimized LiFePO_4 for lithium battery cathodes, *Journal of the electrochemical society* **148**, A224 (2001).
- [11] Z. Cai, B. Ouyang, H.-M. Hau, T. Chen, R. Giovine, K. P. Koirala, L. Li, H. Ji, Y. Ha, Y. Sun, J. Huang, Y. Chen, V. Wu, W. Yang, C. Wang, R. J. Clément, Z. Lun, and G. Ceder, In situ formed partially disordered phases as earth-abundant mn-rich cathode materials, *Nature Energy* **9**, 27 (2024).
- [12] J. Ma, J. Wang, K. Jia, Z. Liang, G. Ji, H. Ji, Y. Zhu, W. Chen, H.-M. Cheng, and G. Zhou, Subtractive transformation of cathode materials in spent li-ion batteries to a low-cobalt 5 v-class cathode material, *Nature Communications* **15**, 1046 (2024).
- [13] K. Wang, Z. Gu, Z. Xi, L. Hu, and C. Ma, Li_3TiCl_6 as ionic conductive and compressible positive electrode active material for all-solid-state lithium-based batteries, *Nature Communications* **14**, 1396 (2023).
- [14] B. Zhu, Z. Lu, C. J. Pickard, and D. O. Scanlon, Accelerating cathode material discovery through ab initio random structure searching, *APL Materials* **9**, 121111 (2021), <https://pubs.aip.org/aip/apm/article->

- pdf/doi/10.1063/5.0076220/14566892/121111_1_online.pdf.
- [15] G. R. Schleder, A. C. M. Padilha, C. M. Acosta, M. Costa, and A. Fazzio, From dft to machine learning: recent approaches to materials science—a review, *Journal of Physics: Materials* **2**, 032001 (2019).
- [16] G. R. Schleder, A. C. M. Padilha, A. Reily Rocha, G. M. Dalpian, and A. Fazzio, Ab initio simulations and materials chemistry in the age of big data, *Journal of Chemical Information and Modeling* **60**, 452 (2020), pMID: 31651163, <https://doi.org/10.1021/acs.jcim.9b00781>.
- [17] S. Batzner, A. Musaelian, L. Sun, M. Geiger, J. P. Mailoa, M. Kornbluth, N. Molinari, T. E. Smidt, and B. Kozinsky, E (3)-equivariant graph neural networks for data-efficient and accurate interatomic potentials, *Nature communications* **13**, 2453 (2022).
- [18] T. Wen, L. Zhang, H. Wang, W. E, and D. J. Srolovitz, Deep potentials for materials science, *Materials Futures* **1**, 022601 (2022).
- [19] M. Rupp, A. Tkatchenko, K.-R. Müller, and O. A. von Lilienfeld, Fast and accurate modeling of molecular atomization energies with machine learning, *Phys. Rev. Lett.* **108**, 058301 (2012).
- [20] A. P. Bartók, M. C. Payne, R. Kondor, and G. Csányi, Gaussian approximation potentials: The accuracy of quantum mechanics, without the electrons, *Phys. Rev. Lett.* **104**, 136403 (2010).
- [21] R. Drautz, Atomic cluster expansion for accurate and transferable interatomic potentials, *Phys. Rev. B* **99**, 014104 (2019).
- [22] J. Peng, J. Du, and L. Wang, The study of ionic conductivity of the li10gep2s12 type solid state electrolyte by an extrapolation method and a deep-learning method, *Journal of Physics: Conference Series* **2557**, 012034 (2023).
- [23] W. Zhang, L. Zhou, T. Yan, and M. Chen, Speciation of $\text{La}^{3+}\text{-Cl}^-$ complexes in hydrothermal fluids from deep potential molecular dynamics, *The Journal of Physical Chemistry B* **127**, 8926 (2023), pMID: 37812657, <https://doi.org/10.1021/acs.jpcc.3c05428>.
- [24] G. Kresse and J. Hafner, Ab initio molecular dynamics for liquid metals, *Phys. Rev. B* **47**, 558 (1993).
- [25] G. Kresse and J. Hafner, Ab initio molecular-dynamics simulation of the liquid-metal–amorphous-semiconductor transition in germanium, *Phys. Rev. B* **49**, 14251 (1994).
- [26] P. E. Blöchl, Projector augmented-wave method, *Phys. Rev. B* **50**, 17953 (1994).
- [27] J. P. Perdew, K. Burke, and M. Ernzerhof, Generalized gradient approximation made simple, *Phys. Rev. Lett.* **77**, 3865 (1996).
- [28] K. Burke, J. P. Perdew, and Y. Wang, Derivation of a generalized gradient approximation: The pw91 density functional, in *Electronic Density Functional Theory: Recent Progress and New Directions*, edited by J. F. Dobson, G. Vignale, and M. P. Das (Springer US, Boston, MA, 1998) pp. 81–111.
- [29] A. I. Liechtenstein, V. I. Anisimov, and J. Zaanen, Density-functional theory and strong interactions: Orbital ordering in mott-hubbard insulators, *Phys. Rev. B* **52**, R5467 (1995).
- [30] S. L. Dudarev, G. A. Botton, S. Y. Savrasov, C. J. Humphreys, and A. P. Sutton, Electron-energy-loss spectra and the structural stability of nickel oxide: An lsd+u study, *Phys. Rev. B* **57**, 1505 (1998).
- [31] J. Zeng, D. Zhang, D. Lu, P. Mo, Z. Li, Y. Chen, M. Rynik, L. Huang, Z. Li, S. Shi, *et al.*, Deepmd-kit v2: A software package for deep potential models, arXiv preprint arXiv:2304.09409 (2023).
- [32] M. Abadi, A. Agarwal, P. Barham, E. Brevdo, Z. Chen, C. Citro, G. S. Corrado, A. Davis, J. Dean, M. Devin, S. Ghemawat, I. Goodfellow, A. Harp, G. Irving, M. Isard, Y. Jia, R. Jozefowicz, L. Kaiser, M. Kudlur, J. Levenberg, D. Mané, R. Monga, S. Moore, D. Murray, C. Olah, M. Schuster, J. Shlens, B. Steiner, I. Sutskever, K. Talwar, P. Tucker, V. Vanhoucke, V. Vasudevan, F. Viégas, O. Vinyals, P. Warden, M. Wattenberg, M. Wicke, Y. Yu, and X. Zheng, TensorFlow: Large-scale machine learning on heterogeneous systems (2015), software available from tensorflow.org.
- [33] L. Zhang, J. Han, H. Wang, W. A. Saidi, R. Car, and E. Weinan, End-to-end symmetry preserving interatomic potential energy model for finite and extended systems, in *Proceedings of the 32nd International Conference on Neural Information Processing Systems, NIPS'18* (Curran Associates Inc., Red Hook, NY, USA, 2018) p. 4441–4451.
- [34] H. Wang, L. Zhang, J. Han, and W. E, Deepmd-kit: A deep learning package for many-body potential energy representation and molecular dynamics, *Computer Physics Communications* **228**, 178 (2018).
- [35] A. P. Thompson, H. M. Aktulga, R. Berger, D. S. Bolintineanu, W. M. Brown, P. S. Crozier, P. J. in 't Veld, A. Kohlmeyer, S. G. Moore, T. D. Nguyen, R. Shan, M. J. Stevens, J. Tranchida, C. Trott, and S. J. Plimpton, LAMMPS - a flexible simulation tool for particle-based materials modeling at the atomic, meso, and continuum scales, *Computer Physics Communications* **271**, 108171 (2022).
- [36] K. Momma and F. Izumi, VESTA: a three-dimensional visualization system for electronic and structural analysis, *Journal of Applied Crystallography* **41**, 653 (2008), <https://onlinelibrary.wiley.com/doi/pdf/10.1107/S0021889808012016>.
- [37] A. Stukowski, Visualization and analysis of atomistic simulation data with ovito—the open visualization tool, *Modelling and Simulation in Materials Science and Engineering* **18**, 015012 (2009).
- [38] K. D. Fong, J. Self, B. D. McCloskey, and K. A. Persson, Onsager transport coefficients and transference numbers in polyelectrolyte solutions and polymerized ionic liquids, *Macromolecules* **53**, 9503 (2020), <https://doi.org/10.1021/acs.macromol.0c02001>.
- [39] N. M. Vargas-Barbosa and B. Roling, Dynamic ion correlations in solid and liquid electrolytes: How do they affect charge and mass transport?, *ChemElectroChem* **7**, 367 (2020), <https://chemistry-europe.onlinelibrary.wiley.com/doi/pdf/10.1002/celec.201901627>.
- [40] A. K. Varshneya, *Fundamentals of inorganic glasses* (Elsevier, 2013).
- [41] D. J. EVANS and G. P. MORRISS, *Statistical Mechanics of Nonequilibrium Liquids* (ANU Press, 2007).